Bioactive glass scaffold architectures regulate patterning of bone regeneration *in vivo*

Xiaomeng Shi[1], Amy Nommeots-Nomm[1], Naomi M. Todd[2], Aine Devlin-Mullin[2], Hua Geng[3], Peter D. Lee[4], Christopher A. Mitchell[2], Julian R. Jones[1*]

1. Department of Materials, Imperial College London, South Kensington Campus London, SW7 2AZ, UK
2. Centre for Molecular Biosciences, University of Ulster at Coleraine, Coleraine BT52 1SA, UK
3. School of Materials, University of Manchester, Manchester, M13 9PL, UK
4. Mechanical Engineering, University College London, London WC1E 7JE, UK

* Corresponding author: julian.r.jones@imperial.ac.uk

ABSTRACT:

The architecture of bone scaffolds, such as pore dimensions, connectivity and orientation can regulate osteogenic defect repair, as can their rate of degradation. Synthetic bone grafts have historically been developed with a foam structures to mimic trabecular bone. Now, Additive Manufacturing techniques enable production of open and regular pore architectures with improved compressive strengths. Here, we compare two types of bioactive glass scaffolds, made of the highly degradable ICIE16 composition, with distinctively different architectures but matched interconnect sizes (~150 μm), produced via two different techniques: gel-cast foaming and direct ink writing. A rabbit lateral femoral defect model was used to compare the effect of their architecture on *in vivo* bone regeneration, relative to a defect only control group, after 4 and 10 weeks of implantation. 3D X-ray microcomputed tomography (micro-CT), correlated to histology and back-scatter electron microscopy (BS-SEM) permitted quantitative evaluation of new bone ingrowth and degradation of the scaffolds. Both foam and printed scaffolds showed equal or higher bone ingrowth compared to the control group. After 4 weeks, the foam group showed the highest osteogenesis, with 51% more bone ingrowth than the defect only controls, but after 10 weeks the defect treated with the printed scaffold had the most bone ingrowth (40% more than the empty defect). Energy dispersive X-ray (EDS) mapping revealed degradation of the glass and calcium-phosphate deposition. The foam group showed more rapid degradation than the printed group, due to higher total porosity (even though interconnected pore size was equivalent). The foam scaffold appeared to allow rapid bone ingrowth and cancellous bone formation, whereas the printed scaffold seemed to provoke cortical-like bone formation, while remaining in place for longer than the 10 week study. While concave architectures promote initial bone ingrowth, the higher strength open pore channels of the printed scaffolds are beneficial for scaffolds made of highly degradable bioactive glasses.

Keywords: Bone ingrowth; additive manufacturing; bioglass; bioactive glass; bone remodelling

1. INTRODUCTION

Bone has an innate capacity for regenerative growth and remodelling, although large bone defects (over approximately 1 cm^3) such as those caused by bone tumour resections and severe non-union fractures cannot fully heal without a template for bone regeneration and/or surgical intervention [1]. The current gold standard treatment is autografting, which involves 'donor' bone from a non-load-bearing site (e.g. the pelvis) transplanted into the defect site [2,3]. However, there are some drawbacks of autografting, such as: donor site pain, limited availability and risk of infection [4].

The original 45S5 Bioglass composition [5] is sold under various product names [6], with the glass being able to promote bone growth through the release of dissolution products [7]. The S53P4 is a variation on this composition and has been successful in the regeneration of bone defects after tumour removal [8] and in treatment of osteomyelitis [9]. Three-dimensional bioactive glass scaffolds, with well controlled architecture, would therefore have the potential to be used as a template for bone regeneration without the drawbacks of autografting [10]. However, Bioglass products are currently particulates and putties: no porous scaffolds are clinically available that retain the amorphous glass network because the glass crystallises on sintering, which can limit performance [11]. New compositions have been developed, such as 13-93 (54.6 SiO_2, 22.1 CaO, 6.0 Na_2O, 1.7 P_2O_5, 7.9 K_2O, 7.7 MgO, in mol%) [12], ICIE16 (49.46 SiO_2, 36.27 CaO, 6.6 Na_2O, 1.07 P_2O_5 and 6.6 K_2O, in mol%) [13] and PSrBG (44.5 SiO_2, 17.8 CaO, 4 Na_2O, 4.5 P_2O_5, 4 K_2O, 8.5 MgO and 17.8 SrO, in mol%) [14] that allowed sintering while maintaining the amorphous structure. The new compositions were designed to widen the sintering window, which is the temperature difference between the glass transition temperature and the crystallisation temperature. Glass particles must be heated to above the glass transition temperature to enable efficient sintering (fusion of the particles by local flow of the glass), but if the temperature reaches the crystallisation temperature, crystallisation can occur that is likely to detrimental to the bioactivity of the device. The aim of the ICIE16 composition was to match the network connectivity (mean number of bridging oxygen bonds per silica tetrahedron) to that of 45S5 Bioglass, while enabling sintering without crystallisation. Bioactive ceramics have been 3D printed into complex architecture[15,16] and the new bioactive glass compositions can now be 3D printed into scaffolds with high strength and open channels [17-19]. However, there are few *in vivo* studies on bioactive glass scaffolds[20] and none have looked at the glass reaction layers in detail.

Our pilot study showed that melt-derived bioactive glass foam scaffolds of the ICIE16 composition encouraged more bone ingrowth than scaffolds of PSrBG bioactive glass after 12 weeks in a rabbit

lateral femoral head defect model [14]. The enhanced performance of ICIE16 bioactive glass foam scaffolds was possibly due to its network connectivity being similar to that of 45S5 Bioglass, whereas PSrBG was higher.

Here, the aim was to investigate how architecture of bioactive glass scaffolds affects bone regeneration by comparing 3D printed grid-like scaffolds to cancellous bone-like foam of the same composition. A previous study compared foamed and printed calcium phosphate scaffolds, but not bioactive glasses [21]. We fabricated ICIE16 bioactive glass scaffolds into two architectures, using the gel-cast foaming and direct ink writing processes. As it was not possible to keep constant both porosity (percentage or pore volume) and interconnect size constant between the scaffold types, we chose to keep interconnect size as the fixed parameter as it determines the width of the path for vascularised bone ingrowth (and cell migration). The gel-cast foaming method uses surfactant to stabilise air bubbles, created by mechanical agitation, in a glass powder and gelatin slurry. In the Direct Ink Writing, or Robocasting, method, "inks" of glass powder mixed with Pluronic F-127 were extruded layer by layer. Sintered scaffolds were implanted into a rabbit lateral femoral head defect model [14]. Here, tomography, electron microscopy and histology were combined to show how the glass reacted *in vivo*. Bone ingrowth and scaffold degradation were quantitatively assessed.

2. MATERIALS AND METHODS

2.1. Glass making

ICIE16 glass frit was produced by mixing the reagents (Table 1) for 8 h (Wheaton mini roller, UK), before melting at 1400°C for 1.5 h in a Pt-5%Au crucible [13]. The melt was then quenched into deionised (DI) water, the glass frit was collected and dried at 100°C. The frit was then ball milled and sieved to yield particles with diameter less than 32 μm.

Table 1. Composition of ICIE16 glass in mol% and its network connectivity (NC') relative to 45S5 Bioglass. NC' refers to the modified network connectivity calculation (mean number of bridging oxygen bonds per silica tetrahedra in the glass structure, calculated from the glass composition [14]).

	SiO_2	CaO	Na_2O	P_2O_5	K_2O	NC'
45S5	46.13	26.91	24.35	2.60		2.11
ICIE16	49.46	36.60	6.60	1.07	6.60	2.13

Scaffolds were produced by gel-cast foaming and 3D printing methods. Both processes use water, for efficient operation of the surfactants. Water has been found to promote glass crystallisation in certain bioactive glass foaming systems [11]. Here, the water exposure was minimised during process

previous optimisation studies and it was found to not affect the final structure of the glasses under the optimised conditions [14,19,22].

2.2. Gel cast foaming of scaffolds

The gel cast foaming process used was that developed previously [14]. 1 g of type-A porcine gelatin (CAS 9000-70-8, Sigma) was dissolved in 20 mL of DI water at 25°C. 25 g of glass powder was then added to form a slurry. Triton X-100 surfactant was added to the slurry and the slurry was foamed under vigorous agitation in air for 2 min (Kenwood hand mixer). The solution was cast into a mould and then placed in an ice bath for 8 min until solidified. The scaffolds were then frozen for 20 min in a -20°C freezer, and transferred to -80°C for 4 h. On removal from the freezer, the scaffolds were freeze dried (CoolSafe 100-4 freeze-drier fitted to a Vacuubrand RZ6 vacuum pump operating at -110°C with an ultimate total vacuum of 1×10^{-2} mbar) for 2 days. Scaffolds were cut with a scalpel to size before sintering to produce samples with dimensions of 6.5 mm diameter and 2 mm depth post sintering. A 2-step sintering cycle was used, holding at 500 °C for 1 h, followed by 690°C for 1.5 h. All sintering processes were conducted at a heating rate of 3°C/min in air. Previous work, including XRD of the scaffolds, showed that this optimised process did not result in crystallisation of the glass [14]. The final morphology of a representative foam scaffold is shown in Figure 1a.

2.3 Direct Ink Writing of scaffolds

In order to prepare the ink for Direct Ink Writing, ICIE16 glass powder was first mixed with 25 wt% Pluronic F-127 solution in volume ratio 45:55. The solution was mixed by using a planetary centrifugal mixer (Thinky mixer ARE-250 USA). Small batches were mixed in individual pots to prevent overheating. Once mixed, the ink was cooled in a 5°C fridge for 15 minutes before more glass was added and remixed, this is repeated until all glass was incorporated. 1 wt% of octanol-1 was added to the final mix to remove the small bubbles within the ink. Once the ink was prepared, the ink was then transferred into a syringe for printing [19].

Printing was completed using a Direct Ink Writing (Robocasting) system (3dInks, USA) with built-in RoboCAD 3.0 (3dInks, USA) software. A pre-designed structure 3D grid-like structure used with strut size: 250 μm; X,Y spacing 160 μm; Z spacing: 250 μm. Scaffolds were printed with dimensions of diameter: ~ 6.48 mm (rows/columns: 44) and thickness: ~ 2.21 mm (layers: 11) via extrusion through a 250 μm conical nozzle (Nordson, UK) under ambient conditions.

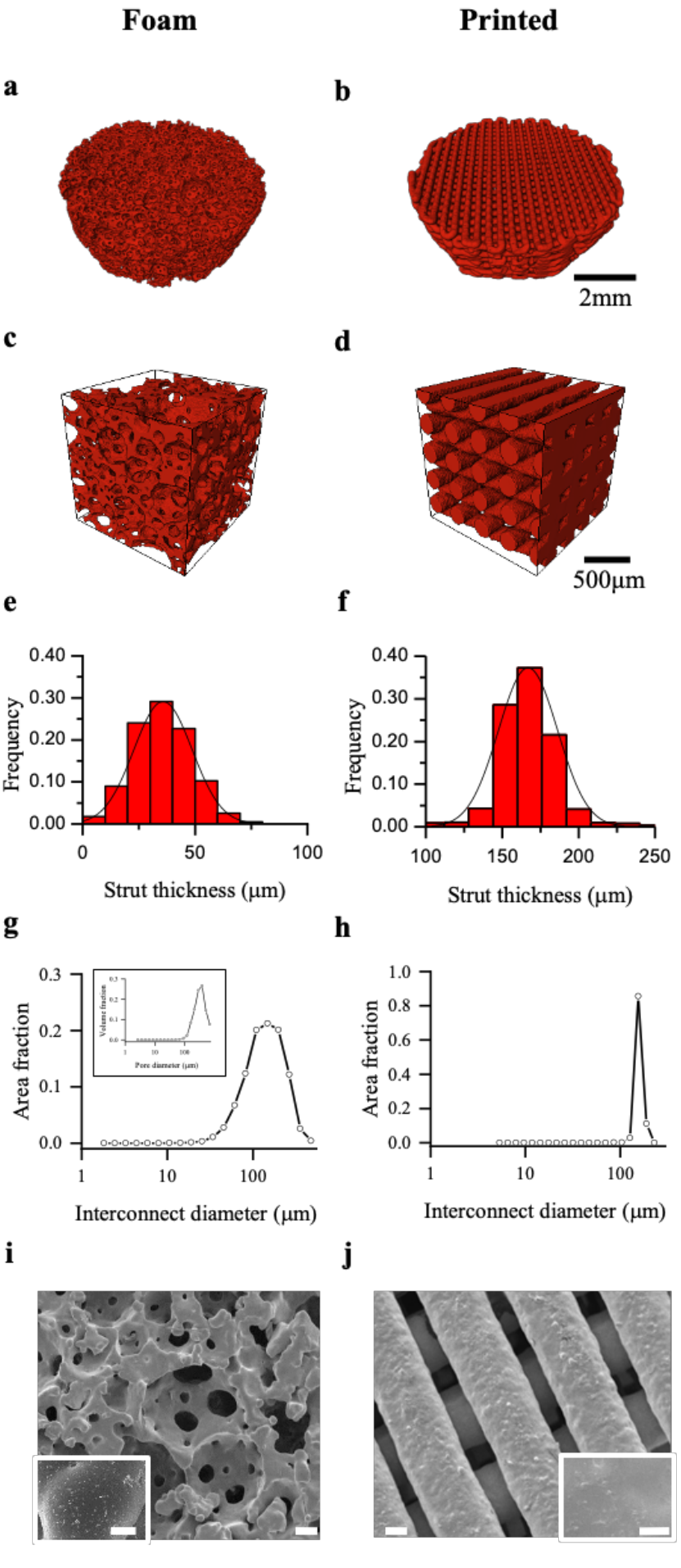
Foam
Printed
a
b
2mm
c
d
500µm
e
f
Frequency
0.40
0.30
0.20
0.10
0.00
0
50
100
Strut thickness (µm)
100
150
200
250
g
h
Area fraction
0.3
0.2
0.1
0.0
1
10
100
Interconnect diameter (µm)
1.0
0.8
0.6
0.4
i
j

Figure 1. Morphology and dimensions of foam and 3D printed scaffolds: Representative µCT 3D renderings of (a) a foam; (b) 3D printed scaffold; (c) zoom in sub-volume of a foam; (d) zoom in sub-volume of a printed scaffold; (e-h) quantification of the µCT images: (e) strut thickness distributions of a representative foam; (f) strut thickness distributions of a representative printed scaffold; (g) interconnect size distribution of a representative foam displayed as area fraction (inset – pore size distribution of a representative foam scaffold displayed as volume fraction); (h) interconnect size distribution of a representative printed scaffold displayed as area fraction; (i) SEM image of a bioactive glass foam scaffold (scale bar 100 µm); inset – higher magnification image of the foam pore wall (scale bar 10 µm); (j) SEM image of a bioactive glass 3D printed scaffold (scale bar 100 µm); inset – higher magnification image of a 3D printed strut (scale bar 10 µm).

Partial overlapping of layers was used to enhance adhesion between the struts, using 80% of the nozzle diameter. The printed scaffolds were then air-dried for 2 days prior to sintering, which was the same as the foam scaffold cycle. Shrinkage was approximately 28 % in the X, Y directions and 18 % in the Z direction. The morphology of a representative printed scaffold is shown in Figure 1b. The printed scaffolds underwent the same sintering profile as foam scaffolds, described in Section 2.2.

2.4. Animal model

All animal procedures were approved and conducted in accordance with institutional (University of Ulster) animal care committee and National (UK Home Office) guidelines. The lateral femoral head defect rabbit model has been previously described in detail [14]. Briefly, 16 female New Zealand half-lop rabbits (2.1–2.8 kg) were used plus 1 rabbit at day 0 for the unoperated and defect only references. In total 17 rabbits were used in this study. Both legs of 16 rabbits (= 32 legs) were used and harvested at either 4 or 10 weeks after surgery (Table 2). Animals were randomly divided into three groups of either five or six rabbits each, corresponding to two different sampling times (4 weeks or 10 weeks).

Table 2. Summary of implanted and control samples used in the rabbit model.

	Composition	Codes	4 weeks	10 weeks
Control	-	Control	6	6
Foam	ICIE16	ICIE16-Foam	5	5
Printed	ICIE16	ICIE16-Printed	5	5

Following appropriate anaesthesia, analgesia and surgical site preparation, a 5 cm incision over the lateral aspect of the knee joint was made with a scalpel. The muscle tissue was blunt dissected, retracted from the underlying bone and connective tissue overlying the lateral aspect of the femoral

condyle was cleared. A 6.5 mm circular defect was drilled in the femoral condyle down to the level of the marrow cavity (with liberal application of sterile saline to prevent heat-induced osteonecrosis) and bleeding minimised by application of pressure. This was performed on both leg of each rabbit. Each defect was either empty (control defect), or filled with either pre-sterilized ICIE16-Foam or ICIE16-Printed cylindrical scaffolds (6.5 mm diameter, 2 mm height). The scaffolds were press fitted into the lesion until they were level with the edge of the remaining bony tissue. Finally, the muscle tissue was re-approximated with 6:0 suture (Ethilon, UK) and the skin was closed with 4:0 suture. Immediately after surgery, the animals received prophylactic topical antibiotics on the surgical site, 5 days of oral antibiotics and had access to fresh green vegetable matter along with standard chow to promote gut health. Pain relief was administered for 3 days post-surgery in the form of oral Metacam.

2.5. Sample extraction

Euthanasia was performed via an overdose of pentobarbitone and subsequently rabbit femoral samples were harvested and cleared of muscle and adherent soft tissue by careful dissection. Samples were then fixed in 10% neutral buffered formalin solution (Sigma, UK) for at least one week. After fixation, each sample was individually wrapped in Parafilm M (Bemis, USA) and placed in a 50 mL falcon tube (VWR, USA) prior to µCT scanning.

2.6. µCT scanning procedure

Five representative foam scaffold and five printed samples were scanned using a laboratory-based µCT system (Nanofocus, Phoenix|X-ray General Electric Company, Measurement and Control, Wunstorf, Germany). The scans were operated at 70 kV and 140 µA, resulting in an image matrix of 1989 x 1989 x 1000 pixels with an isotropic voxels size of 4.4 µm. Excised femora with empty defects (n = 12), foam (n = 10) or printed bioactive glass (n = 10) subsequent to implantation (*vide supra*) were also µCT scanned according to this protocol. Images were reconstructed using the Datos|x software, resulting in an image matrix of 1989 x 1989 x 1000 pixels with an isotropic voxels size of 18.9 µm.

2.7. µCT Analysis

All images were analysed using Avizo software (Avizo 9.0, FEI Visulization Sciences Group, Mérignac Cedex, France) and Matlab (Mathworks Inc., Natick, Massachusetts, USA). For the scaffold itself, the strut size distribution of each individual foam scaffold (n = 10) and printed scaffold (n = 10) was calculated using a 3D distance map [23]. The interconnect size distribution of foam and printed scaffold and the pore size distribution of foam scaffold were obtained by in-house

developed watershed algorithm-based methods [23-28]. Due to the characteristic of straight pore channel of printed scaffold, the channel size can also be represented by the interconnect size. Specific surface area (SSA) of scaffold (scaffold area/mass of scaffold) was also measured.

For the rabbit femur samples, the reconstructed data were first normalised to a predetermined reference histogram, followed by a smoothing filter (median filter) to reduce the noise and artefacts. The μCT datasets were then segmented into three phases: bone, scaffold and background (including soft tissue) to quantify the extent of bone ingrowth and scaffold degradation during the time periods selected. Two global thresholds were applied to separate the background from the rest, and the bone and from the scaffold.

In order to compare equivalent regions between different samples, a cylindrical mask (6.5 mm in diameter and 3 mm in height) which had the same diameter but was 1 mm thicker than the scaffolds was applied to the defect site of each individual sample respectively. The overlapping of the femur sample dataset and cylindrical mask [29] were used to generate a reproducible region of interest (ROI), (Figure 2). Only bone and scaffolds within this mask were used for the quantification. Total bone formation was determined by normalising the volume of new bone to the available volume in the ROI. The 3D quantification of new bone formation and scaffold degradation was calculated using following rules:

Percentage of newly formed bone within the ROI:

$$\% \text{ newly formed bone} = [\text{bone vol.}/(\text{ROI vol.} - \text{scaffold vol.})] \times 100$$

Percentage of scaffold degradation was calculated by subtracting the remaining scaffold volume from the initial scaffold volume prior to implantation:

$$\% \text{ scaffold degradation} = [(\text{initial scaffold vol.} – \text{final scaffold vol.})/\text{initial scaffold vol.})] \times 100$$

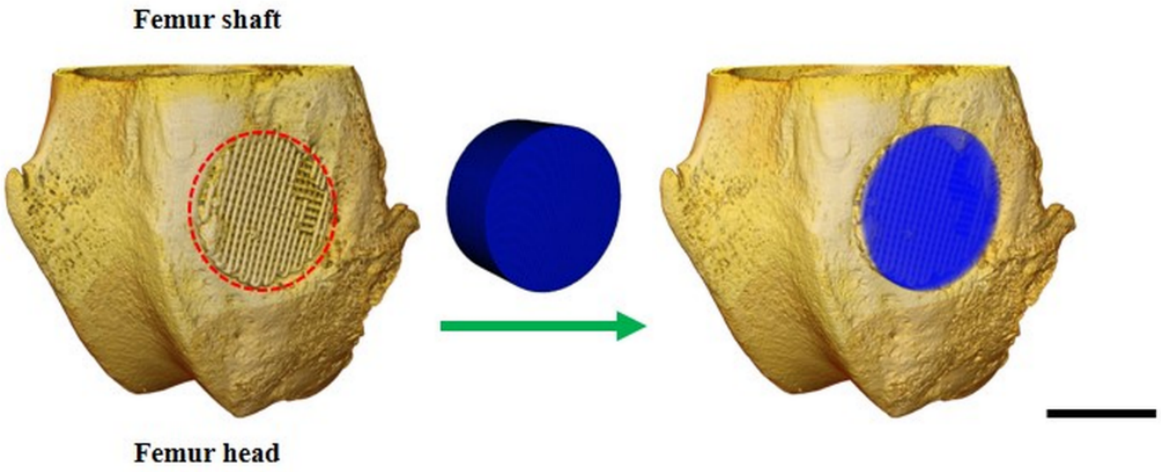

Figure 2. 3D rendered µCT image of a rabbit femur head defect model containing an implanted 3d printed scaffold (left) and a 6.4 x 3 mm cylindrical mask (blue) used as ROI. The red dashed circle indicates the defect site. Scale bar = 5 mm.

2.8. Histology

After µCT scanning, single samples from each group and time-point (total 6 samples) were cut into 1.5 mm thick pieces through the defect site using a 0.3 mm thick IsoMet™ Diamond Wafering Blades (Buehler, USA). The cut samples were then dehydrated through a series of increasing concentrations of ethanol and embedded in LR white resin (TAAB Laboratories Equipment Ltd, UK) for sectioning. The tissue blocks were then ground successively with K800, K2000, and K4000 grinding paper using a Struers grinding system to expose and polish the surface of the femur. The polished surface was then glued onto an acrylic disc (30 mm diameter/4 mm thick – made in-house). The tissue block was then ground with the same series of grinding paper resulting in a sample ~50-100 µm-thick. All sections were stained with Gill's Haematoxylin III (Sigma-Aldrich, UK) and Eosin (Sigma-Aldrich, UK) according to the manufacturer's protocol. Sections were placed in 1% formic acid (Sigma-Aldrich, UK) for 2 minutes, rinsed in absolute ethanol for 5 minutes, and then rinsed in deionized water for another 5 minutes. Haematoxylin solution was applied dropwise onto the bone section for 15 min and then rinsed with tap-water. Eosin solution was added for 10 min followed by another rinse in water and subsequent air-drying. Stained samples were then examined on a Fixed Stage Microscopes BX51 (Olympus, Japan) at a range of objective magnifications.

2.9. Scanning Electron Microscopy (SEM)

Samples from each group, at each time point, were also sectioned into 1.5 mm thick pieces. They were dehydrated, resin embedded, ground, and polished in exactly same as described for histology but using epoxy resin (Buehler, IL, USA). SEM images of transverse cross sections of bone implant

rabbit femur samples were acquired using a LEO 1525 Field Emission Scanning Electron Microscope (Zeiss, Germany) using an automatic stitching system, Autostitch [30,31], which automatically stitches local images together to form an image of the entire sample. Back-scatter SEM (BS-SEM) observations were made at 20 kV to assess the morphology of newly formed bone and scaffold at either 4 and 10 week implantation in both foam and printed scaffold samples. The elemental presence was analysed with energy dispersive X-ray spectroscopy (EDX) to monitor the chemical reaction of ICIE16 glass scaffolds. All five elements of ICIE16 glass: Si, Ca, P, Na, and K were detected for both ICIE16-Foam and ICIE16-Printed in 4 and 10 week time point samples.

2.10. Statistical analyses

All the results from SEM-EDX and μCT are presented as mean ± standard deviation. Statistical comparisons were performed with a Mann-Whitney U test. All statistical analysis was carried out using XLSTAT (Addinsoft, Inc., USA) with statistical significance considered when $p \leq 0.05$(*).

3. RESULTS

3.1. Characterization of ICIE16 bioactive glass scaffolds.

Both foam and printed scaffolds were made such that their modal interconnect size, as determined from μCT image analysis of five of each type of scaffolds, was as similar as possible (Table 3): 139.5± 11.6 for the foams and 153.3 ± 6.4 for the printed scaffolds. Architectures of the foamed and printed scaffolds are shown in Figure 1a-d. Printed scaffolds had a narrower interconnect and pore size distribution than the foams, due to the regular nature of the pore channels enabled by the extrusion printing process. The foaming process produced a wider interconnect size distribution: ranging from 1.9 μm to 452.2 μm as the windows between spherical pores, which had a modal spherical pore diameter of 338.5 ± 61.4 (Figure 1g-h). In the printed scaffolds, the pore size and the interconnect size were equivalent, due to the channel-like nature of the pores. The foam scaffolds also exhibited a higher surface area, but lower relative density and thinner strut size than printed scaffolds (Figure 1e,f; Table 3). SEM images show that the interconnects of the foams (Figure 1i) and pore channels of the printed scaffold (Figure 1j), with higher magnification images showing a roughness to both the foam and printed scaffolds (insets). Previous work, using 4D μCT, showed that the struts almost completely densified, but some spherical pore inclusions remained [22]. As the spherical pores in the foam are larger than the connections between them, in order to match the interconnect diameter to that of the printed scaffolds the foams had a higher percentage porosity of 74.8 ± 1.7 % compared to 46.4 ± 3.3 % (Table 3). Compressive strengths of the scaffolds were measured previously to be 3.4 ± 0.3 MPa for the foam scaffolds [14] and 32.5 ± 8.1 MPa for the printed scaffolds [19].

Table 3. Summary of characterisation of the foamed and printed scaffolds following analysis of µCT images.

	Surface Area (mm^2)	Specific surface area (cm^2/g)	Modal strut thickness (µm)	Modal interconnect size (µm)	Modal pore size (µm)	Porosity (%)
Foam	901.9 ± 132.8	176.3 ± 19.9	35.8 ± 13.0	139.5 ± 11.6	338.5 ± 61.4	74.8 ± 1.7
Printed	810.9 ± 99.1	76.0 ± 7.9	166.9 ± 19.4	153.3 ± 6.4	—	46.4 ± 3.3

3.2. µCT-based quantification of bone regeneration and scaffold degradation

The extent of bone ingrowth into the control defects and into foam and printed scaffolds were imaged via µCT, SEM and histological images after 4 and 10 weeks. µCT scans of the entire rabbit femoral heads were taken and reconstructed in 3D (Figure 3). 2D representative images through the centre of the defect are shown in Figure 3 to qualitatively demonstrate bone growth over time, which had occurred in all groups to some extent by 4 weeks. In the empty defect (Figure 3e,f), bone ingrowth had occurred but it was limited to the outer part of the bone, where the cortical bone had been prior to surgery (cortical bone region, Figure 3a,b) and it had not yet formed a complete bridge across the defect. In the foam and printed groups, the original morphological structure of the scaffolds was still visible after 4 weeks' implantation. In the foam scaffolds, bone had grown in from the periphery, in towards the centre of the cylinder in the defect but did not quite reach the centre (Figure 3i,j). More bone grew in that it did into the empty defect. Only a small amount of bone grew into the 3D printed scaffold (Figure 3m,n) by 4 weeks.

After 10 weeks, an increase in the amount of new bone regeneration was observed relative to 4 weeks, in all cases. The control defects did show some bone ingrowth that connected across the diameter (and through the centre) of the defect site, (Figure 3g,h), but now the bone was bridging at a lower point in the defect, in the cancellous bone part of the femur, away from the cortical bone region. Defects that contained the foam scaffolds (Figure 3k,l) showed a similar pattern of bone ingrowth to the control, with the bone bridging away from the cortical region an incomplete pattern of bone formation, leaving a small region at the defect centre unrepaired. The scaffolds had completely biodegraded. Small regions of high X-ray attenuation may be remaining fragments of the foam scaffold 10 weeks of implantation (Figure 3, yellow arrow heads). The 3D printed scaffolds were still present after 10 weeks with bone ingrowth occurring from the periphery to the centre of the defect (Figure 3o,p) and bridged through the centre of the defect. Again, the bone ingrowth bridged in the same region as the empty

defect. The μCT images qualitatively showed both foam and printed scaffold structures were capable of supporting bone regeneration in the rabbit femur head defect model.

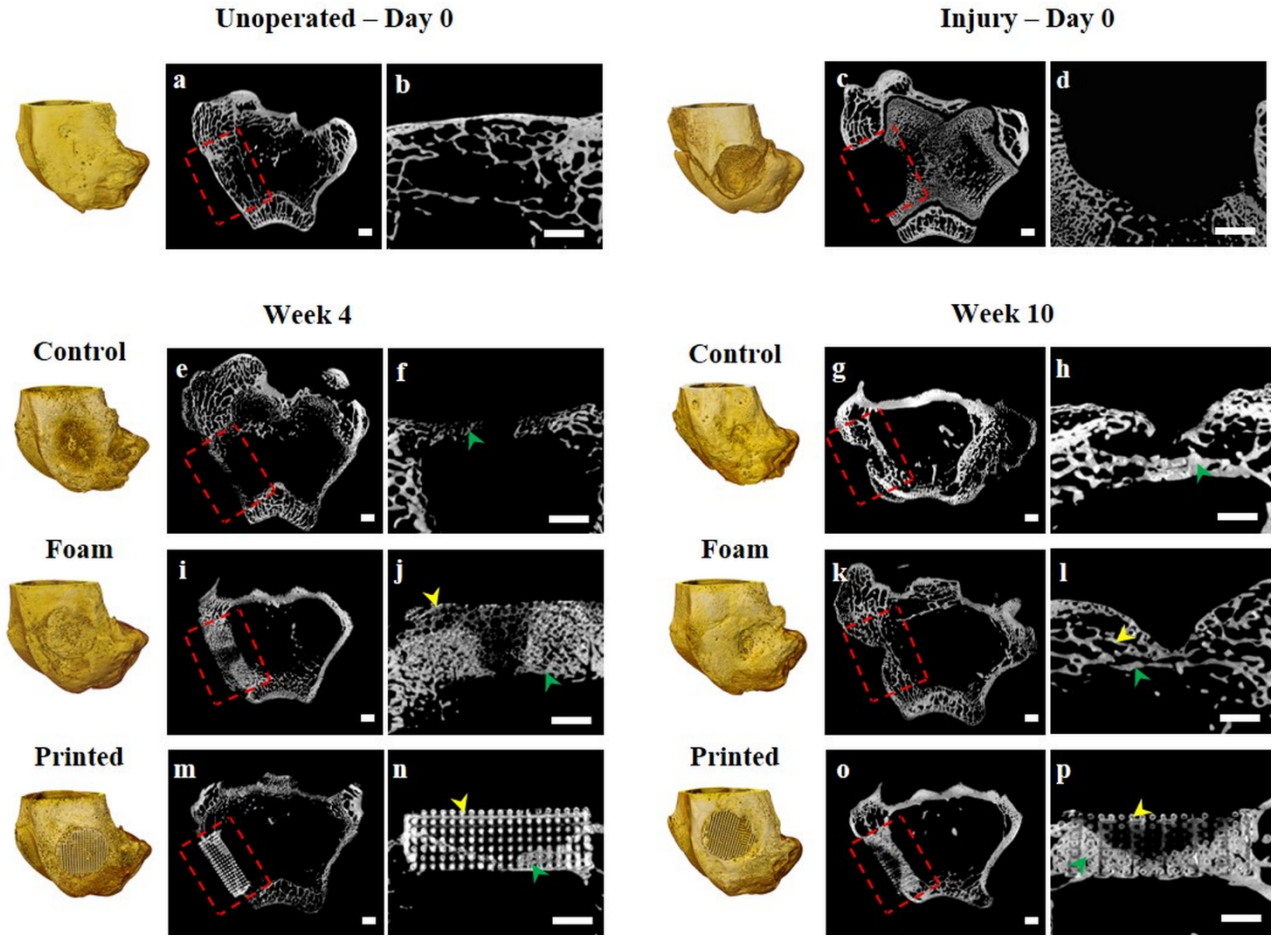

Figure 3. 3D reconstructions and 2D defect centre slices of μCT images of rabbit femoral condyle defects: (a,b) un-operated rabbit femoral condyle; (c,d) empty defect without scaffolds at day 0 (immediately post-surgery); (e-h) 2D slices of control defects (not implanted with scaffolds) after 4 and 10 weeks; (i-l) 2D slices of defect sites implanted with ICIE16 foam scaffolds after 4 and 10 weeks; (m-p) 2D slices of defect sites implanted with ICIE16 printed scaffolds after 4 and 10 weeks. Within the defect region (red boxes), new bone formation (examples indicated by green arrowheads) and possible undissolved scaffold material (examples indicated by yellow arrowheads) are distinguishable. Scale bar = 1mm.

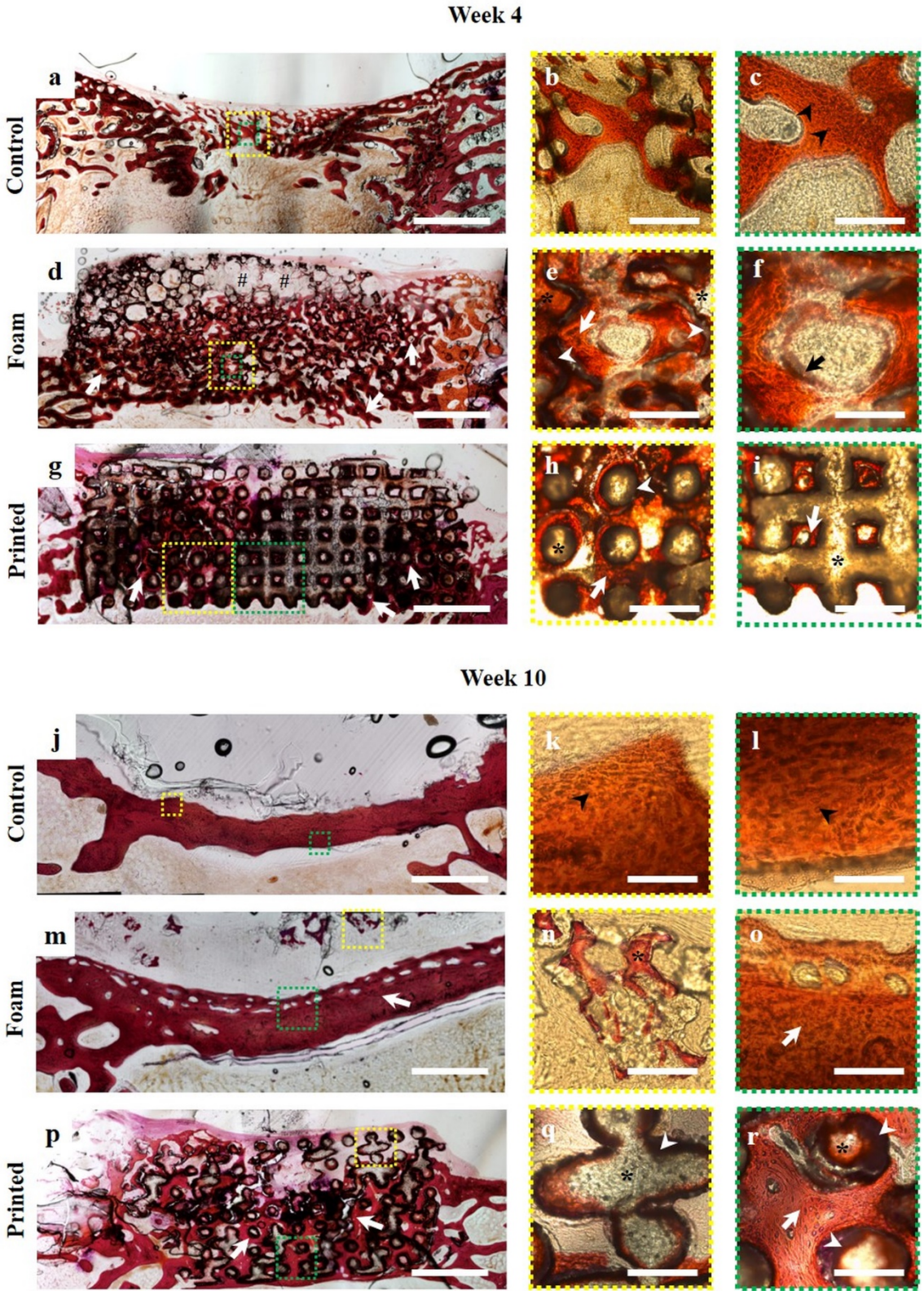

Figure 4. Light microscopic images of Haematoxylin and Eosin stained transverse sections (50-100 µm) of control lesions (a-c; j-l), foam (d-f; m-o) or printed scaffolds (g-i; p-r) from implant sites in rabbit lateral femoral condyles sampled at 4 weeks (a - h) or 10 weeks (i – r) after surgery. Scale bars = 125 µm (c, f, k, l), 250 µm (b, e, n, o, q, r), 500 µm (h, i), 1000 µm (a, d, g, j, m, p). Insets correspond to higher magnification of the dashed boxes. White arrows indicate bone formation; black arrows indicate presumptive connective tissue; black arrowheads indicate trapped osteogenic cells; white arrowheads indicate apatite-like formation of bioactive glass; *= glass scaffold; # identifies regions of glass degradation.

To validate that the bone identified in μCT was actually bone, histological examination of H&E stained sections was carried out. Sections from 4 week control samples revealed that thin layer of spongy cancellous-like bone spanning the defect site, which was contiguous with the pre-existing peripheral bone (Figure 4a). Bone ingrowth is sparse towards the centre of the defect (Figure 4a,b), although the regenerated bone did contain mineralized deposits (Figure 4b) and numerous encapsulated osteogenic cells (black arrowheads in Figure 4c). They are assumed to be osteogenic cells as they are encapsulated in bone matrix and are the appropriate size.

In foam scaffolds at 4 weeks **(**Figure 4d), a thin layer of newly formed bone, with close apposition to glass, spanned the entire depth and width of the lesion. There is evidence of glass degradation of some struts, particularly those in outer areas external to the lesion site (#) and also where new bone contacted the mineralized scaffold surface (Figure 4e,f). Bone infiltration is contiguous with the periphery (Figure 4e: white arrows) and a layer of what could be connective tissue is also seen within some pores (Figure 4f: black arrow).

In printed samples at 4 weeks, there is evidence of robust bone ingrowth at the periphery of the scaffold (Figure 4g,h; white arrows) while it is more sparse bone at the scaffolds centre (Figure 4i), with features consistent with peripheral (hydroxyapatite) mineralization (Figure 4h: white arrowheads) and central degradation of strut architecture (Figure 4i: asterisk). New bone was particularly conspicuous around cylindrical struts (Figure 4h) and in concave pores **(**Figure 4i).

At 10 weeks after surgery (Figure 4j), dense cortical-like bone spanned the entire lesion site in the controls with trapped osteocytes visible (Figure 4k,l: black arrowheads), with little evidence of cancellous bone architecture. The bone in this section appears different to those seen in the μCT and SEM images because this section was not from the geometric centre of the defect, in contrast to where the μCT slice and section imaged by SEM were taken. In foam implants, the majority of the scaffold material is no longer visible (degraded) and mature new bone **(**Figure 4m,o: white arrows) was present, although some persistent glass (yellow boxed inset) was observed on the external aspect of the injury site (Figure 4n)**.** In printed scaffolds (Figure 4p-r) after 10 weeks, there was extensive new bone formation (white arrows) throughout the scaffold, contiguous with the host bone (Figure 4p,r). Intense eosinophilic staining of scaffold material, particularly around the periphery of struts and strut intersections was observed (Figure 4p,q), consistent with hydroxyapatite formation. Glass conversion to apatite was thinner at the extremities (Figure 4q: white arrowheads) and thicker in regions contacted by new bone (Figure 4r: white arrowheads).

The next step was quantification of the new bone formation (Figure 5a) and scaffold resorption (Figure 5b). A predefined cylindrical with diameter 6.5 mm and height 3 mm was chosen as our defined ROI for ingrowth (Figure 2). At week 4, foam implants showed increased bone ingrowth (31.1 ± 5.3%) compared to control (20.6 ± 2.8%) and 3D printed (22.1 ± 3.3%) groups (Figure 5a). After 10 weeks, the ROI for the control defects and those that had contained the foam had similar proportions of new bone ingrowth with 25.8 ± 1.4% and 25.6 ± 3.2% of available volume replaced by new bone respectively. The reason why bone ingrowth percentage at 10 weeks was less than at 4 weeks is because the foam scaffold largely degraded after 10 weeks, which increased the total available volume. In contrast, the proportion of new bone in the 3D printed group significantly increased ($p<0.05$) from 22.1 ± 3.3% at 4 weeks' implantation to 36.3 ± 4.6% at 10 weeks.

The proportion of scaffold resorption is summarized in Figure 5b. Higher degradation was observed for the foam scaffolds compared to printed scaffolds. The foam scaffolds degraded 27.4 ± 9.1% compared to the printed scaffolds degrading 7.7 ± 2.4% of their initial volume by 4 weeks. The degradation of the foam scaffolds increased to 95.3 ± 4.7%, which means almost all the scaffolds was resorbed. Only 34.9 ± 8.3% of printed scaffolds degraded after 10 weeks, retaining the framework structure of the scaffolds.

In order to quantify the extent and variation of circumferential bone ingrowth into the cylindrical ROI, μCT ROI datasets at 10 week were sub-divided into three equal thickness concentric subvolumes of interest (VOIs): outer, middle and central (Figure 5c: right panel). The proportion of new bone was highest in the outermost VOI for all 3 groups (Figure 5c: left), which is consistent concentric ingrowth of new bone from outside the implant. The proportion of bone present decreased towards the centre of the ROI (Figure 5c: left). However, the printed group showed much significantly higher relative bone ingrowth ($p < 0.05$) into the outer and middle VOIs compared to the control and foam implanted groups (most of the foam scaffold was no longer present), although there were no significant differences in bone ingrowth into the central VOI.

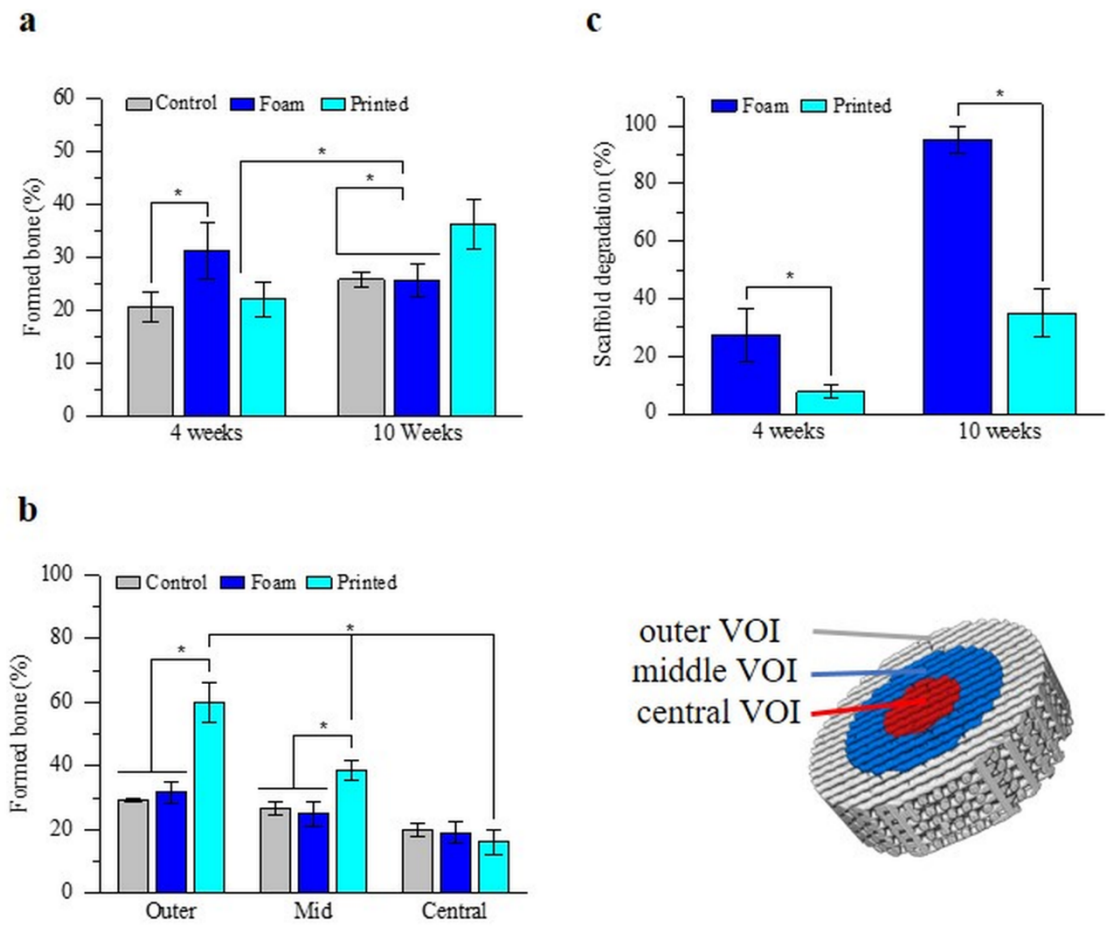

Figure 5. Quantification of bone ingrowth into the pre-defined ROI at 4 and 10 weeks post-implantation: (a) the percentage of ROI that was newly formed bone; (b) percentage of scaffold degradation; c) schematic of the ROI cylinder (right) divided into subvolumes of interest (VOIs) at 10 weeks post- implantation and a bar graph (left) of the percentage of newly formed bone within the three VOIs. Data is represented as mean ± sd (minimum of 5 samples).

3.3. Micro-scale new bone formation and scaffold degradation using SEM

Figure 6 shows representative defect low magnification BS-SEM images of full sections from the defect and higher magnification images of new bone and implant interfaces. The red arrowheads and yellow arrowheads indicate the new bone and residual implants respectively. The overall regeneration and integration pattern of new bone formation observed from SEM images was consistent with observations from μCT, in that the control defects did not completely bridge at 4 weeks, but did at 10 weeks, whereas bone ingrowth into the scaffolds was higher. At 10 weeks, the foam was no longer visible and the bone bridging was on the interior side of the implant. The printed scaffold provoked dense cortical bone like ingrowth at the inner marrow/cancellous bone side of the scaffold, high ingrowth at 10 weeks and slower degradation/remodelling of the scaffold (Figure 6d).

An interesting observation, was that new bone formation preferred to form on the concaved pores of the foam scaffold and the concave features of the printed scaffold, i.e. corners of the pore channels, indicated by the red arrowheads in Figure 6c,e,f.

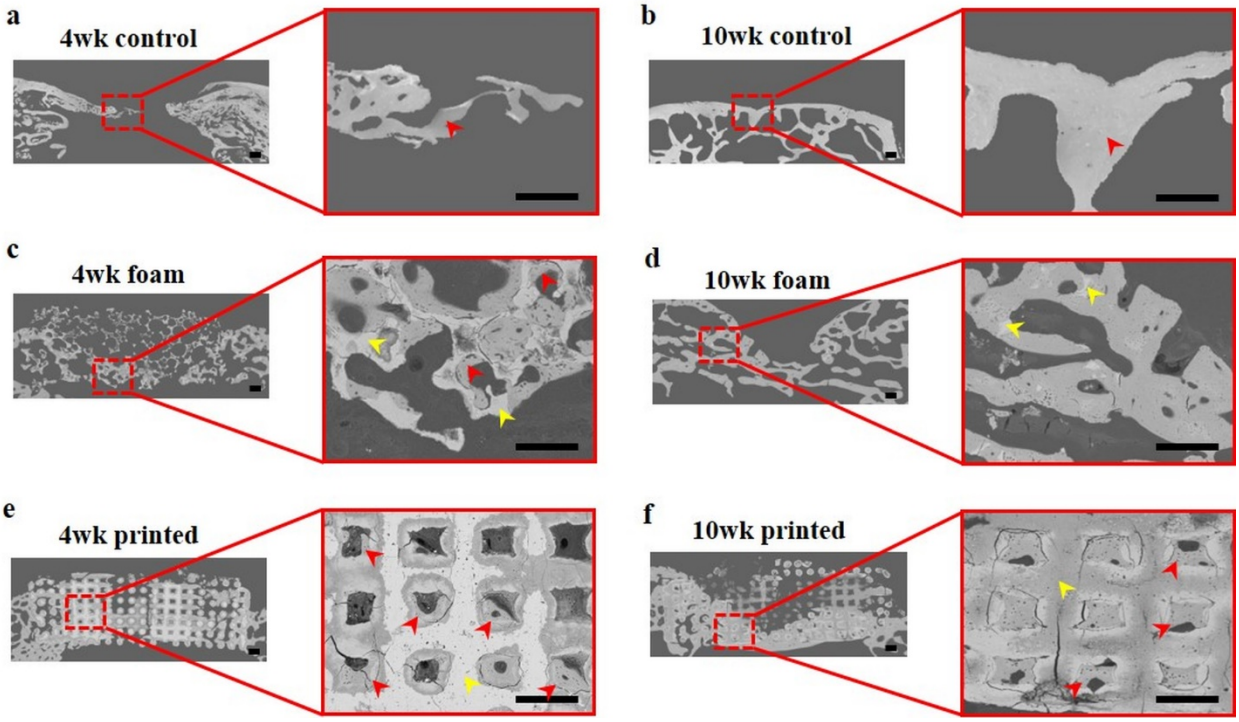

Figure 6. Low and high magnification of BS-SEM images of the defect sites: (a) 4 week control; (b) 10 week control; (c) 4 week foam; (d) 10 week foam; (e) 4 week printed; (f) 10 week printed. The brighter regions of BSE the images indicate material with higher average atomic number than darker regions. Red arrowheads indicate new bone ingrowth particularly in concavities adjacent to scaffold material; yellow arrowheads indicate the remaining scaffold. Scale bar = 400 µm.

3.4. Elemental mapping of newly formed bone and scaffolds

Formation of new bone and conversion and degradation of bioactive glass implants in rabbit femoral defect was examined by BS-SEM using and EDX mapping for elemental distribution. The heterogeneous distribution Si, Ca, P, Na and K observed at 4 and 10 weeks' post-implantation (Figure 7) revealed different stages of new bone formation and chemical conversion of the implants.

In the control group, elemental mapping (Figure 7a,b) showed the newly formed bone had a very similar elemental composition compared to the host bone (taken away from the defect, not shown in Figure 7). In the foam group, two phases were observed after 4 weeks' post implantation (Figure 7c). The central region (phase 1) of the foam scaffold had lower silicon and higher phosphorus (Figure 7c) content compared to original composition ICIE16 glass. No silicon was observed in the outer region (phase 2) but instead, a high proportion of calcium and phosphorus was deposited in this region, resulting in a calcium phosphate-rich region, which had a very similar Ca:P ratio to the

new bone formed on the surface of the foam scaffold strut. At 10 weeks, the central region observed in week 4 disappeared, leaving only one homogeneous calcium phosphate-rich region (Figure 7d), indicating complete conversion to apatite.

In the printed group, after 4 weeks post-implantation, the printed scaffold strut turned into 3 distinctive concentric phases (Figure 7e): a calcium phosphate-rich layer (region 3: ~50 μm thick), an SiO_2-rich layer (region 2: ~150 μm thick) and a central region (1) which had similar similar atomic weight to the original ICIE16 glass (Figure 7e). A strong signal of silicon was observed in the intermediate region (phase 2) with a small amount calcium and phosphorus, suggesting a partially dissolution of the glass strut with only the glass former remaining and most of the modifier element were released. No evidence of silicon was found in the outer region (phase 3). In contrast, strong signals of calcium and phosphorus were detected in this region, making it a calcium phosphate-rich layer. After 10 weeks, only 2 out of 3 phases remained (Figure 7e). The central original glass region was no longer present, with only a partially dissolved glass region and calcium-phosphate rich region remaining, indicating that the strut was only a silica-rich glass covered in apatite, i.e. most cations had been ion exchanged. It was also worth noting that in both groups, the bone tissue bonded directly to the outer converted layer.

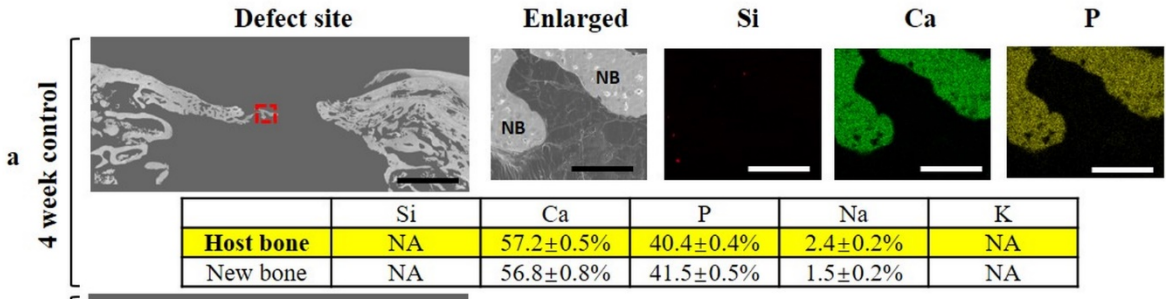

	Si	Ca	P	Na	K
Host bone	NA	57.2±0.5%	40.4±0.4%	2.4±0.2%	NA
New bone	NA	56.8±0.8%	41.5±0.5%	1.5±0.2%	NA

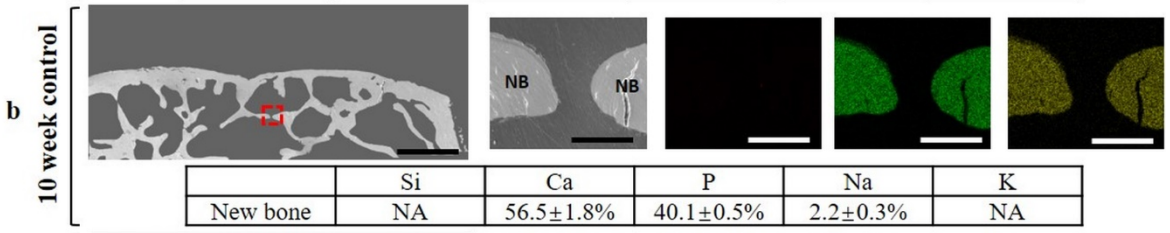

	Si	Ca	P	Na	K
New bone	NA	56.5±1.8%	40.1±0.5%	2.2±0.3%	NA

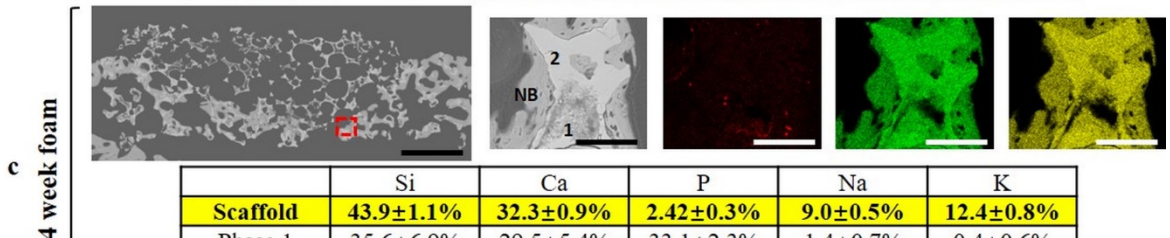

	Si	Ca	P	Na	K
Scaffold	**43.9±1.1%**	**32.3±0.9%**	**2.42±0.3%**	**9.0±0.5%**	**12.4±0.8%**
Phase 1	35.6±6.9%	29.5±5.4%	33.1±2.3%	1.4±0.7%	0.4±0.6%
Phase 2	NA	55.3±0.3%	42.7±0.3%	2.1±0.1%	0.1±0.0%
New bone	NA	56.1±0.6%	41.8±0.6%	2.1±0.1%	0.1±0.0%

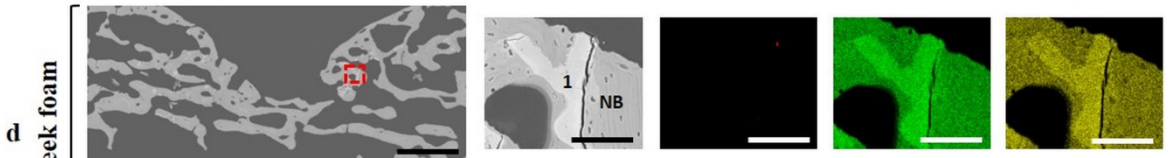

	Si	Ca	P	Na	K
Phase 1	NA	56.4±0.6%	40.1±0.5%	3.7±0.5%	NA
New bone	NA	55.9±0.6%	41.0±0.8%	3.4±0.4%	NA

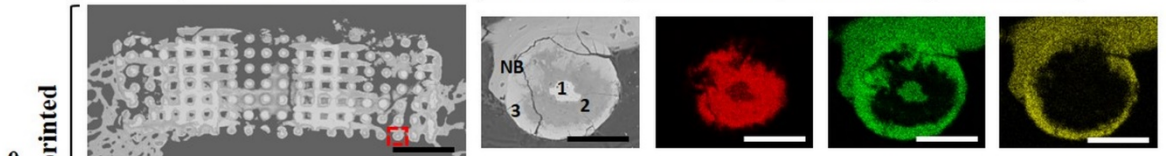

	Si	Ca	P	Na	K
Phase 1	43.8±0.4%	32.3±0.5%	2.6±0.2%	9.7±0.2%	11.6±0.3%
Phase 2	80.6±3.8%	10.1±2.0%	8.8±1.6%	0.1±0.1%	0.1±0.1%
Phase 3	2.9±1.1%	55.2±1.7%	39.5±1.4%	1.4±0.2%	0.1±0.2%
New bone	NA	54.9±0.4%	41.9±0.5%	2.6±0.2%	0.1±0.1%

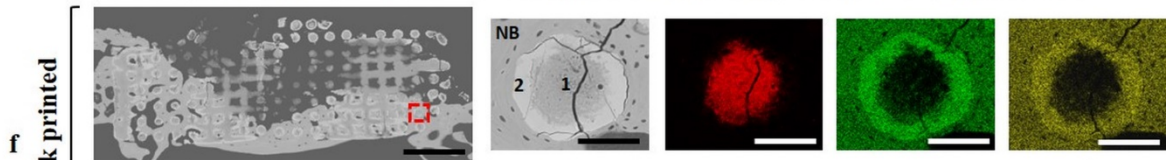

	Si	Ca	P	Na	K
Phase 1	78.0±6.6%	11.2±3.8%	10.1±2.8%	0.4±0.2%	NA
Phase 2	4.7±3.1%	52.3±1.8%	39.4±1.6%	2.3±0.2%	0.1±0.0%
New bone	NA	55.8±1.3%	40.4±0.6%	2.7±0.8%	0.1±0.1%

Figure 7. BS-SEM (left) and EDX elemental maps of new bone of control (a and b), and of new bone and the implant for foam (c and d) and printed (e and f) implants after 4 and 10 weeks' implantation. The red dashed boxes identify enlarged regions on which the mapping was performed. Brightness of colour (Si: red; Ca: green; and P: yellow) corresponds to

abundance of each element within the enlarged area. The atomic weight of elements (Si, Ca, P, Na, and K) of the mother bone and original scaffold (highlighted in yellow) and new bone and different phases (marked with number) of the scaffolds (shown in enlarged images) is presented in the tables beneath the corresponding SEM images respectively. The data was obtained by taking 6 points at each phase. Scale bar = 1 mm (whole defect region BS-SEM images), scale bar = 100 µm (enlarged images).

4. DISCUSSION

4.1 The extent of osteogenesis

Both foam and printed ICIE16 scaffolds supported bone regeneration in a rabbit femoral head defect and improved the bone regeneration pattern compared to defect only control by 10 weeks. The different architectures of the scaffolds had a strong impact on how new bone grew into the implant and the integration of the implant and the host bone (Figure 3). While larger pores are expected to allow more bone ingrowth [32], here the windows between which bone can grow were kept the same between the scaffolds.

After 4 weeks' post-implantation, new bone regeneration was found predominantly at the periphery of the foam scaffolds with good integration though the contact between the foam scaffold surface and host bone. At 10 weeks, higher bone regeneration was observed compared to 4 weeks. Only a thin layer of new bone formed on the marrow cavity side of the implant/defect site. The 3D printed scaffolds initially showed less bone ingrowth from the host bone than the foam scaffolds at 4 weeks. But after 10 weeks, the printed scaffolds showed an increase in bone regeneration with more cortical-like bone and a thicker region of bone formation, again at the marrow cavity side of the defect site (Figure 3). While the foam had almost completely biodegraded, the printed scaffold remained largely intact, although the glass had undergone extensive dissolution and apatite formation (Figure 7). The foam biodegraded faster due to the higher total porosity (75% compared to 46% for the printed scaffolds) and thinner strut sizes. The more rapid dissolution of the foams is unlikely to be due to differences in density of the pore walls, compared to the 3D printed struts, as high magnification imaging showed no pores in the foam walls (Figure 1i), but has shown some isolated intra-strut spherical pores in the 3D printed scaffolds[22]. The more rapid degradation of the foam will likely have released more active ions into the defect region, even though total available ions (glass) per cubic centimetre of scaffold would have been less for the foam, due to its lower relative density. The concave pores and rapid ion release may have provoked rapid bone ingrowth into the foam. Similar results were observed when osteogenesis in printed and foamed calcium phosphate scaffolds was compared [21].

Here, the bone integration pattern in the two groups of scaffolds was different and may result from differences in the scaffold architecture. Previous studies have shown that not only pore size, but also porosity, interconnect size, permeability, tortuosity, and microstructural anisotropy of the scaffolds can have strong impact on new bone integration [20,33,34]. Here, the bone ingrowth pattern from the foam implant may relate to the relatively faster degradation rate of the foam scaffold (in comparison to printed) which almost fully dissolved by 10 weeks, giving no support and guidance to the new bone ingrowth. This would explain why the bone ingrowth pattern at 10 weeks was similar to the control defect group which had no support implant during the repair period. The slow degradation rate of the printed scaffold seems to provide continued support and guidance, as well as more sustained ionic release to the new bone.

The new bone seemed to initial formed at the concave side or corner of the pores or pore channels (e.g. red arrows in Figure 6). This was observed in both the foam and printed groups at both time points and has previously been observed in other biomaterials, including synthetic hydroxyapatite that releases ions much slower than these bioactive glasses [35,36]. Nonetheless, the preferential bone formation could still be due to concentration of dissolution products at concavities, in part due to reduced local fluid flow, resulting in higher local concentration of Ca^{2+} [21,24,37] or Si (when present) [38] at the corners/concavities. It could also be due to changes in surface energy due to the microtopography and pore curvature [39]. Protein adsorption the scaffold surface which facilitates cell is determined by scaffold surface properties; these include surface chemistry, charge, free energy and stiffness [40]. In the cases of foam and printed scaffolds, local stiffness was constant, although the compression modulus of the scaffold would vary due to the differences in total porosities.

When Liu et al. [20] implanted bioactive glass foam-like scaffolds in rat calvarial defects, they saw approximately 10 % more pore volume filled by new bone in scaffolds with columnar-like pores compared to cancellous-like, with the new bone entering the scaffolds at the bottom (*dura* side). Here, we observed similar behaviour in our femoral model, in that the new bone formed first from the periphery and bone marrow (bottom) side of the scaffolds (Figure 3o,p, Figure 6d). The bone marrow is the primary source of stem cells that can progress down an osteogenic route and a source for new blood vessel growth, which can provide oxygen and nutrients as well as supporting metabolism during new bone formation. However, the foam scaffolds encouraged more rapid initial bone ingrowth than the oriented pores. The bone distribution was not clear once the foams had degraded at 10 weeks, but for the printed scaffolds, the bone remained towards the base of the scaffolds and was dense.

4.2 Mineralisation and degradation of scaffolds in vivo

Bioactive glass is a material that can convert to an HCA-like substance *in vivo* [20,41,42]. Previously, ICIE16 foam scaffolds were shown to form an HCA-like layer on the surface of the scaffold after 1 week immersion in simulated body fluid (SBF) *in vitro*, but the chemical reaction of ICIE16 scaffold *in vivo* and further replacement of scaffold by bone is an unknown. Interestingly, the printed scaffolds in this study followed the classic sequence of events proposed by Hench [20,41]: silica-rich layer formation, due to cation exchange followed by calcium phosphate deposition that can crystallise into HCA. The new bone formation showed close apposition to the scaffold, implying very little fibrous tissue formation. The foam scaffold sample followed the same trend as the printed scaffold. However, since the foam scaffold had thinner struts and a higher specific surface area than printed scaffold, the overall transformation rate was much faster for this architecture. After 4 weeks, there was no silica-rich region remaining in foams (Figure 6c) and a thick layer of calcium-phosphate formed on the surface. The calcium-phosphate ratio of this layer (1.3:1) was similar to the calcium-phosphate layer formed in the printed scaffold (1.4:1). At the centre of scaffold, a calcium-phosphate region with different calcium-phosphate ratio (0.9:1) was also detected. The region was probably still in the process of transforming into the final HCA form. After 10 weeks, all of the foam scaffold was completely converted to HCA-like material and fully surrounded by new bone, indicating that silicate dissolution continued even though an HCA shell formed. This has previously been attributed to the mineral shell being remodelled by cellular resorption allowing for transport of soluble silica through an incomplete shell [43,44]. Liu et al. reported that the presence of Si in the converted HCA layer of 13-93 bioactive glass scaffolds, with a concentration gradient from the SiO_2-rich interior to the surface of the implant. Here, a small amount of Si was observed in the HCA layer, but no concentration gradient was found, this may be related to the faster degradation of ICIE16 compared to 13-93.

4.3 Implant degradation

The rate of degradation of scaffolds plays a key role in cell stimulation and bone regeneration [45-47]. Here, scaffold degradation provides calcium and phosphate ions need to form HCA-like surface for bone bonding, but also ions for osteogenic stimulation. Once the bioactive glass is converted, and HCA is formed, the converted glass is gradually replaced by new bone due to the remodelling process [48,49]. The speed of the remodelling process largely depends on the contact area between bone and converted glass scaffold. Too much degradation of the scaffold may impair bone regeneration, especially where this occurs before it has completed its' structural support or templating role [46,50].

When comparing bone ingrowth between the groups at 4 weeks, foams showed the highest percentage of new bone formation compared to either defect only or printed groups (Figure 5a): the foam scaffold had the highest degradation, which was almost 4 times faster than the printed scaffold. The rapidly released ions, including soluble silica, Ca^{2+} and PO_4^{3-}, could be a reason for the rapid formation of new bone in foam group. The foam glass scaffold is almost completely degraded and replaced by new bone after 10 weeks, matching the 6 week bone remodelling period of rabbit [51]. In comparison, only a third of the printed scaffolds was degraded after 10 weeks, and there was a thick layer of HCA-like material on their surface. An optimal scaffold for bone regeneration, therefore might include a foam-like region for rapid bone ingrowth and ion release for osteogenic stimulation, adjacent to a 3D printed region of higher compressive strength and slower resorption that encourages cortical-like bone formation. Such a structure could be conceived through AM methods, perhaps using a gyroid structure rather than a conventional foam.

5. CONCLUSIONS

Two types of bioactive glass scaffolds of the same glass composition and interconnect pore size were successfully fabricated and implanted into rabbit lateral femoral defect and the nature of bone regeneration imaged and quantified in 2D and 3D by μCT. After 4 weeks, the foam group showed the highest amount of bone ingrowth compared with control and printed groups but was surpassed by the 3D printed scaffolds after 10 weeks, at which point the foam scaffold had almost fully degraded/ remodelled. The 3D printed scaffold remained at 10 weeks and bone with dense cortical-like morphology spanned the defect, through the scaffold. The results suggest that a combination of foam and printed architectures s could be suitable for the repair of bone defects, with the foams encouraging rapid regeneration and the printed scaffolds providing a longer term scaffold with higher strength and higher bone density.

6. ACKNOWLEDGEMENTS

The authors gratefully acknowledge funding from the EPSRC (EP/I020861/1); the Department of Materials (Imperial College London); the MRC (MR/R025673/1) and facilities for the Research Complex at Harwell. AD-M was funded by a DEL/CAST Award from the University of Ulster. PDL acknowledges support from a Royal Academy of Engineering Chair in Emerging Technology. Raw data is available on request from rdm-enquiries@imperial.ac.uk.

REFERENCES

1. Stevens, M. M., *Materials Today* (2008) **11** (5), 18
2. W Bauer, T., and Muschler, G., *Clinical Orthopaedics and Related Research* (2000) **371**, 10
3. Kucera, T.*, et al.*, *European Journal of Orthopaedic Surgery & Traumatology* (2012) **22**, 123

4. Younger, E. M., and Chapman, M. W., *Journal of Orthopaedic Trauma* (1989) **3** (3), 192
5. Hench, L. L.*, et al.*, *J Biomed Mater Res Symp* (1971) **2** (1), 117
6. Jones, J. R.*, et al.*, *Int J Appl Glass Sci* (2016) **7** (4), 423
7. Xynos, I. D.*, et al.*, *J. Biomed. Mater. Res.* (2001) **55** (2), 151
8. Lindfors, N. C.*, et al.*, *J. Biomed. Mater. Res. Part B* (2010) **94B** (1), 157
9. Lindfors, N. C.*, et al.*, *Bone* (2010) **47** (2), 212
10. Jones, J. R., *Acta Biomaterialia* (2013) **9** (1), 4457
11. Wu, Z. Y.*, et al.*, *Acta Biomater* (2011) **7** (4), 1807
12. Brink, M., *J. Biomed. Mater. Res.* (1997) **36** (1), 109
13. Elgayar, I.*, et al.*, *J. Non-Cryst. Solids* (2005) **351** (2), 173
14. Nommeots-Nomm, A.*, et al.*, *Acta Biomaterialia* (2017) **57**, 449
15. Feng, C.*, et al.*, *ACS Biomaterials Science & Engineering* (2020)
16. Zhang, W.*, et al.*, *Biomaterials* (2017) **135**, 85
17. Fu, Q.*, et al.*, *Adv. Funct. Mater.* (2011) **21** (6), 1058
18. Fu, Q.*, et al.*, *Acta Biomater* (2011) **7** (10), 3547
19. Nommeots-Nomm, A.*, et al.*, *Journal of the European Ceramic Society* (2018) **38** (3), 837
20. Liu, X.*, et al.*, *Acta Biomaterialia* (2013) **9** (1), 4889
21. Barba, A.*, et al.*, *ACS Applied Materials & Interfaces* (2017) **9** (48), 41722
22. Nommeots-Nomm, A.*, et al.*, *Mater. Today Adv.* (2019) **2**, 9
23. Yue, S.*, et al.*, *Acta Biomater* (2011) **7** (6), 2637
24. Jones, J. R.*, et al.*, *Biomaterials* (2007) **28** (7), 1404
25. Atwood, R. C.*, et al.*, *Scripta Materialia* (2004) **51** (11), 1029
26. Jones, J. R.*, et al.*, *Philosophical Transactions of the Royal Society A: Mathematical, Physical and Engineering Sciences* (2006) **364** (1838), 263
27. Yue, S.*, et al.*, *J Mater Sci: Mater Med* (2010) **21** (3), 847
28. Midha, S.*, et al.*, *Acta Biomaterialia* (2013) **9** (11), 9169
29. Geng, H.*, et al.*, *J. Mater. Sci. - Mater. Med.* (2016) **27** (6), 9
30. Brown, M., and Lowe, D., *International Journal of Computer Vision* (2007) **74** (1), 59
31. Brown, M., and Lowe, D., Recognising panorams. Presented at International Conference on Computer Vision, (2003)
32. Hing, K. A.*, et al.*, *J. Mater. Sci. - Mater. Med.* (1999) **10** (10-11), 663
33. Jones, A. C.*, et al.*, *Biomaterials* (2009) **30** (7), 1440
34. Otsuki, B.*, et al.*, *Biomaterials* (2006) **27** (35), 5892
35. Ripamonti, U.*, et al.*, *Matrix* (1992) **12** (3), 202
36. Hing, K. A.*, et al.*, *J. Biomed. Mater. Res. Part A* (2004) **68A** (1), 187
37. Klar, R. M.*, et al.*, *Journal of Cellular and Molecular Medicine* (2013) **17** (11), 1444
38. Hing, K. A.*, et al.*, *Biomaterials* (2006) **27** (29), 5014
39. Zhao, G.*, et al.*, *Biomaterials* (2007) **28** (18), 2821
40. von Recum, A. F., and van Kooten, T. G., *Journal of Biomedical Science. Polymer Edition* (0920-5063 (Print))
41. Hench, L. L., *Journal of the American Ceramic Society* (1991) **74** (7), 1487
42. Rahaman, M. N.*, et al.*, *Acta Biomaterialia* (2011) **7** (6), 2355
43. Schepers, E. J. G., and Ducheyne, P., *Journal of Oral Rehabilitation* (1997) **24** (3), 171
44. Radin, S.*, et al.*, *Journal of Biomedical Materials Research* (0021-9304 (Print))
45. Kim, J. A.*, et al.*, *Acta Biomaterialia* (2016) **44**, 155
46. Barradas, A. M.*, et al.*, *European cells & mateirals* (1473-2262 (Electronic))
47. Yoon, J. J., and Park, T. G., *Journal of Biomedical Materials Research* (2001) **55** (3), 401
48. Midha, S.*, et al.*, *Advanced Healthcare Materials* (2013) (2192-2640 (Print))
49. ten Harkel, B.*, et al.*, *PLoS One* (2015) **10** (10), e0139564
50. Boonrungsiman, S.*, et al.*, *Proceedings of the National Academy of Sciences* (2012) **109** (35), 14170
51. Roberts, E. W., Bone Physiology, Metabolism, and Biomechanics In *Contemporary Implant Dentistry*, 3rd ed.; Misch, C. E., (ed.) Mosby Elsevier((2008)), pp 324